The Cryosphere Discussions

Remote sensing of sea ice: advances during the DAMOCLES project

G. Heygster[1], V. Alexandrov[2], G. Dybkjær[4], F. Girard-Ardhuin[3],
W. von Hoyningen-Huene[1], I. L. Katsev[5], A. Kokhanovsky[1], T. Lavergne[6],
A. V. Malinka[5], C. Melsheimer[1], L. Toudal Pedersen[4], A. S. Prikhach[5], R. Saldo[7],
R. Tonboe[4], H. Wiebe[1], and E. P. Zege[5]

[1]Institute of Environmental Physics, University of Bremen (UB), Germany
[2]Nansen International Environmental and Remote Sensing Centre (NIERSC), St. Petersburg,
Russia and Environmental and Remote Sensing Centre, Bergen, Norway
[3]Institut Français de Recherche pour l'Exploitation de la Mer (IFREMER), Plouzané, France
[4]Danish Meteorological Institute (DMI), Denmark
[5]B.I. Stepanov Institute of Physics of the National Academy of Sciences of Belarus (IP-NASB),
Minsk, Belarus
[6]Norwegian Meteorological Institute (met.no), Oslo, Norway
[7]Danish National Space Center (DNSC), Copenhagen, Denmark

Abstract

In the Arctic, global warming is particularly pronounced so that we need to monitor its development continuously. On the other hand, the vast and hostile conditions make in situ observation difficult, so that available satellite observations should be exploited in the best possible way to extract geophysical information. Here, we give a résumé of the sea ice remote sensing efforts of the EU project DAMOCLES (Developing Arctic Modeling and Observing Capabilities for Long-term Environmental Studies). The monthly variation of the microwave emissivity of first-year and multiyear sea ice has been derived for the frequencies of the microwave imagers like AMSR-E and sounding frequencies of AMSU, and has been used to develop an optimal estimation method to retrieve sea ice and atmospheric parameters simultaneously. A sea ice microwave emissivity model has been used together with a thermodynamic model to establish relations between the emisivities at 6 GHz and 50 GHz. At the latter frequency, the emissivity is needed for assimilation into atmospheric circulation models, but more difficult to observe directly. A method to determine the effective size of the snow grains from observations in the visible range (MODIS) is developed and applied. The bidirectional reflectivity distribution function (BRDF) of snow, which is an essential input parameter to the retrieval, has been measured in situ on Svalbard during the DAMOCLES campaign, and a BRDF model assuming aspherical particles is developed. Sea ice drift and deformation is derived from satellite observations with the scatterometer ASCAT (62.5 km grid spacing), with visible AVHRR observations (20 km), with the synthetic aperture radar sensor ASAR (10 km), and a multi-sensor product (62.5 km) with improved angular resolution (Continuous Maximum Cross Correlation, CMCC method) is presented. CMCC is also used to derive the sea ice deformation, important for formation of sea ice leads (diverging deformation) and pressure ridges (converging). The indirect determination of sea ice thickness from altimeter freeboard data requires knowledge of the ice density and snow load on sea ice. The relation between freeboard and ice thickness is investigated based on the airborne Sever expeditions conducted between 1928 and 1993.

1 Introduction

Sea ice is an essential component of the climate system at high latitudes. It influences weather and climate on both regional and global scales. Sea ice is an efficient insulator that strongly reduces fluxes of heat and vapour between ocean and atmosphere, where even small fractures in the Actic sea ice may double the heat flux between ocean and atmosphere (Rampal, 2008; Andersen et al., 2007). The combination of thinning Arctic sea ice and the positive albedo feedback mechanism, caused by relative low albedo of the open ocean, the signal of global warming is amplified in the Arctic (Serreze et al., 2009). Sea ice extent, concentration, drift and deformation are therefore important parameters to both coupled climate circulation models and for operational applications like numerical weather prediction. These characteristics must be monitored continuously. The goal of this review is to combine into a bundle the progresses of the sea ice remote sensing capabilities achieved during the project DAMOCLES (Developing Arctic Modeling and Observing Capabilities for Long-term Environmental Studies) conducted from 2006 to 2010. DAMOCLES was one of the main European contributions to the International Polar Year.

For observing sea ice from space, passive microwave sensors have the advantages of being independent of the day/night condition and widely independent of cloud cover. Moreover, their availability since 1972 makes passive microwave observations the longest of all satellite records available and allows for analyses on climate time scales. However, the amount of emitted radiation (radiance) is much higher and varies much more than the one of open water, making it difficult to estimate areas covered by the main sea ice type (first-year ice or multiyear ice) and to determine atmospheric quantities from microwave observations over sea ice. The necessary step to improve this situation of better estimating the microwave emissivity at the microwave observing frequencies is presented in Sect. 2.1, together with an application to retrieve both surface and atmospheric parameters over sea ice. As an attempt to predict the sea ice emissivity from the meteorological history, Sect. 2.3 combines a sea ice emissivity model

with a thermodynamic model, driven with ECMWF atmospheric model data (Tonboe, 2010).

Knowledge of the sea ice temperature is required to determine the energy flux between ocean and atmosphere. It is relevant when retrieving the microwave emissivity (see above), and is needed to determine the atmospheric temperature profile from data of temperature sounders like AMSU-B. In thermodynamic equilibrium, the vertical temperature profile within the sea ice and snow pack is characterized by the snow surface temperature (IST, ice surface temperature) and the snow/ice interface temperature SIIT. Section 3 investigates the relation between these two quantities and the brightness temperatures, together with a study investigating which microwave frequencies are best suited as proxies for assimilation in atmospheric circulation models.

Snow on top of the sea ice is little in mass, but crucial for all climate change studies because not only the area covered by snow and ice is reduced with time (Seidel and Martinec, 2004), but also the snow strongly influences the albedo of the sea ice, and thus the local radiative balance which plays an essential role for the albedo feedback process. The albedo of snow does not have a constant value, but depends on the grain size, with smaller grains having higher albedo, and the amount of pollution like soot (e.g. in Eurasia; Nazarenko and Hansen, 2004) and in fewer cases dust which both lower the albedo significantly. DAMOCLES has contributed to our remote sensing capabilities for the snow grain size (Sect. 4.1), which is based on the knowledge of the reflectance function (Sect. 4.2) and to the retrieval of the albedo itself (Sect. 4.3).

Sea ice drift and deformation are dynamic parameters influencing the open water fraction and ice thickness distribution and hence the energy and mass balance of the Arctic sea ice. Section 5 presents progresses in the detection of sea ice drift and deformation derived from the METOP instruments scatterometer ASCAT, the optical radiometer AVHRR and from ASCAT (Advanced Synthetic Aperture Radar) on ENVISAT.

The thickness of sea ice is needed to determine the ice volume, compute the ice mass exchanges with the ocean, to validate numerical models of the ocean circulation as well as to plan ship and offshore operations in the ice. In the last 10 yr, radar

Title Page

Abstract | Introduction

Conclusions | References

Tables | Figures

◄ | ►

◄ | ►

Back | Close

Full Screen / Esc

Printer-friendly Version

Interactive Discussion

altimeter data from ERS and ENVISAT have been used to determine the inter-annual changes in sea ice thickness through direct measurements of sea ice freeboard. The contribution of DAMOCLES, presented in Sect. 6, was an investigation on the relation between freeboard and ice thickness based on the airborne Sever expeditions con-
⁵ ducted between 1928 and 1993.

2 Sea ice microwave emissivity

2.1 Emissivity determination

The satellite observed radiance, called brightness temperature $T_b = T_{em} \times \varepsilon$, is the product of the physical temperature T_{em} of the emitting layer and the emissivity ε, a mate-
¹⁰ rial parameter. Over open ocean, microwave observations have been used for many decades to determine a wide range of surface and atmospheric parameters. Over sea ice, we so far only have been able to retrieve concentrations (percentage of surface cover) of total ice and multi-year ice (ice having survived at least one summer melt season). The reason why we can extract so much less geophysical information from
¹⁵ microwave observations over sea ice is the high and highly varying sea ice emissivity, making it difficult to determine the much smaller atmospheric component of the received radiation. Moreover, the microwave radiation emanates, compared to water, from much deeper layers of snow and ice, where the meteorological history is frozen in the microphysical parameters, resulting in a much more complex relationship be-
²⁰ tween physical properties of the snow/ice complex and the microwave radiances. As a consequence, reliable emissivity forward models, while existing for open water, remain a challenge for the case of sea ice. As an additional difficulty, in winter the high vertical temperature gradient within the sea ice from about $-30\,°C$ at the surface to $-1.8\,°C$ at the bottom complicates the determination of the temperature of the emitting
²⁵ layer at the different observing frequencies which span the range from 6 to 183 GHz and have different penetration depths. Within DAMOCLES, the emissivities of first-year and multiyear sea ice, the two most prominent ice types, were determined at

all microwave observing frequencies of the sensors Advanced Microwave Sounding Unit (AMSU) (Matthew et al., 2008) and Advanced Microwave Scanning Radiometer on EOS (AMSR-E) (Matthew et al., 2009). In both studies, the emissivity is retrieved over two Arctic regions, one covered by first-year ice (76.5° N–78° N, 77° E–79° E) in the Kara Sea and one covered by multiyear ice (84° N–85.5° N, 31.5° W–36° W) north of Greenland. Knowledge about the surface temperature and atmospheric temperature and humidity profiles is provided from ECMWF re-analysis data. Vertical temperature profile within the snow and sea ice pack are taken from the Heat Budget of the Arctic Ocean (SHEBA) observations in 1998 and 1999 (Moore et al., 2002) and penetration depth data from Haggerty and Curry (2001) are used to estimate the temperature of the emitting layer, using a linear regression.

Here we present as examples the monthly averaged results for first-year ice (Fig. 1) and multiyear ice (Fig. 2) for the AMSR-E frequencies ranging from 7 to 89 GHz. During the winter months, the surface emissivity and the concentrations of first-year ice shown also in Fig. 1 are near unity and the difference between horizontally and vertically polarized emissivity is low. During the months of June, July, and October, the satellite footprints may contain both ice and open water, leading to high variability (error bars) of the determined average emissivity. During August and September, the ice has completely melted, and the emissivity of open water is observed. The monthly variation of multi-year ice (Fig. 2) remains nearly constant for all months except the summer months from May to September when the higher values are observed, with a maximum of 0.95 at 7 GHz in June. The retrieved emissivities agree well with those of AMSU. For the first time, also the correlations between the emissivities at different frequencies and polarizations of AMSR-E have been determined (Mathew et al., 2009). The covariances, which are easily derived from the correlations, are required when assimilating the brightness temperatures into atmospheric and ocean circulation models.

As an application, the method was transferred to data of the atmospheric temperature sounder AMSU-A within the operational processing chain of met.no (Schyberg and Tveter, 2009, 2010).

Another important application of the emissivities is the retrieval of atmospheric parameters over sea ice, similarly as has been done over open ocean from passive microwave sensors for more than three decades. The idea is to model the radiances of the AMSR-E channels with a forward model that takes surface and atmospheric parameters as input, and then use an inverse method to retrieve these parameters (state variables) from the measured AMSR-E radiances. The state variables here are: surface wind speed, total column water vapour (TWV), cloud liquid water path (CLW), sea surface temperature, ice surface temperature, sea ice concentration, and multiyear ice fraction.

The forward model is based on the one by Wentz and Meißner (2002) which simulates AMSR-E radiances over open water given wind speed, TWV, CLW, and surface temperature. We have modified this forward model to allow partial or full ice cover of the sea. This in turn requires knowledge of the sea ice emissivity of first-year ice and multiyear ice which is taken from the method described above.

The inverse method, the "optimal estimation method" (Rodgers, 2000), requires a priori data and covariances for all state variables. The a priori data for the ice concentration are directly determined from the AMSR-E brightness temperatures (using the NASA Team algorithm), the a priori surface temperatures are derived from the AMSR-E brightness temperatures, the ice concentration and the sea ice emissivities. The remaining a priori data are taken from meteorological analysis data (ECMWF). The solution has to be found by an iteration scheme (Newton method), and comprises not just the retrieved state variables, but also includes the a posteriori covariance matrix which contains the standard deviations (the error) of the retrieved variables and their mutual correlations.

The retrieval produces fields (swath by swath) of the state variables. The entire Arctic can be covered daily. However, mainly in areas of multiyear ice, the retrieval shows slow convergence – the most probable reason is that the emissivities of multiyear ice are not well enough represented in the forward model, as they are based on emissivity values retrieved for a certain area ($85° N–85.5° N$, $31.5° W–36° W$, see above).

2.2 Emissivity modelling; combination with thermodynamic model

In DAMOCLES the microwave emission processes from sea ice have been simulated using the combination of a one dimensional thermodynamic sea ice model and a microwave emission model (Tonboe, 2010; Tonboe et al., 2011). The emission model is the sea ice version of the Microwave Emission Model for Layered Snow-packs (MEMLS) (Wiesmann and Mätzler, 1999; Mätzler et al., 2006).

It has been demonstrated that the seasonal variability of thermal microwave emission can be simulated using a combination of thermodynamic model and emission modelling. Both emissivity at 18, 36 and 89 GHz, its temporal variability, the gradient ratio at 18 and 36 GHz ($GR_{18/36} = (T_{18v} - T_{36v})/(T_{18v} + T_{36v})$) and the polarisation ratio at 18 GHz ($PR_{18} = (T_{18v} - T_{18h})/(T_{18v} + T_{18h})$) are comparable to typical signatures derived from satellite measurements (Tonboe, 2010).

The correlation between the multiyear ice brightness temperature (T_v), emissivity (e_v) and effective temperature (T_{eff}) at 18, 36 and 50 GHz is high ($r \geq 0.94$) and the correlation between 18 and 36 GHz multiyear ice e_v, T_{eff} and T_v is equally good for high and low physical temperatures. These lower frequencies penetrate into the multiyear ice while the penetration of the 89 GHz reaches only to the snow ice interface. The high frequency channels at 150 and 183 GHz are penetrating only the snow surface and the correlation between these is also high ($r = 0.99$). The emissivity of multiyear ice e_{v89} in between the high and low frequency channels is relatively poorly correlated to its frequency neighbours. For cases with little extinction in the snow, the microwave penetration at 89 GHz is to the snow-ice interface. For cases with deeper snow or stronger extinction in the snow, the 89 GHz emission is primarily from the snow. The shift between the two emission regimes can strongly influence T_{v89} and its correlation to neighbours. Figure 3 shows the emissivity at 18, 36 and 89 GHz and vertical polarisation vs. the emissivity at 50 GHz.

The emissivity is affected by volume scattering processes in the snow cover and upper ice. The $GR_{18/36}$ which is a measurable proxy for scattering is further related to

Title Page

Abstract | Introduction

Conclusions | References

Tables | Figures

|◄ | ►|

◄ | ►

Back | Close

Full Screen / Esc

Printer-friendly Version

Interactive Discussion

the emissivity of multiyear ice $e_{v\,50}$ at 50 GHz. The linear relationship between these two simulated parameters seems to be robust over the wide range of temperatures and snow depths covered by the cases of Fig. 3. However, the relationships of T_{eff} to measurable parameters such as air or surface temperature show less correlation because of the steep temperature gradient near the surface and the penetration depth variability. Nevertheless, T_{eff} is highly correlated with that of neighbouring channels. The simulated relationship between $GR_{18/36}$ and $e_{v\,50}$ suggests that it may be possible to estimate the microwave emissivity at the atmospheric sounding frequencies ($\sim$50 GHz) from satellite measurements at lower frequencies seasonally across the Arctic Ocean with microwave instruments such as SSMIS as it is done over open water. The emissivity of the sounding frequencies cannot be detected directly from observations in these channels because they are dominated by the atmospheric signal component which in addition is difficult to separate from the surface contribution.

Test runs with the regional numerical weather prediction model HIRLAM where satellite microwave radiometer data from sea ice covered regions were assimilated indicated that atmospheric temperature sounding of the troposphere over sea ice, which is not practiced in current numerical weather prediction models, is feasible. The test showed that the assimilation of Advanced Microwave Sounding Unit (AMSU) near 50 GHz temperature sounding data over sea ice improved model skill on common variables such as surface temperature, wind and air pressure. These promising test results are the motivation for the new EUMETSAT's Ocean and Sea Ice Satellite Application Facility (OSI SAF) sea ice emissivity model.

The OSISAF emissivity model is based on simulated correlations between the surface brightness temperature at 18 and 36 GHz and at 50 GHz. The model coefficients are tuned with simulated data from a combined thermodynamic and emission model in DAMOCLES. The intention with the model is to provide a first guess sea ice surface emissivity estimate for tropospheric temperature sounding in numerical weather prediction models assimilating both AMSU and Special Sensor Microwave Imager/Sounder (SSMI/S) data (Tonboe and Schyberg, 2011).

3   Sea ice temperature

The snow surface temperature is among the most important variables in the surface energy balance equation and it significantly affects the atmospheric boundary layer structure, the turbulent heat exchange and the ice growth rate. It is an important parameter in itself for assimilation in numerical weather prediction models and coupled ocean-sea ice hydrodynamic models.

The snow surface on thick multiyear sea ice in winter is on average colder than the air because of the negative radiation balance (Maykut, 1986). Beneath the snow surface there is a strong temperature gradient with increasing temperatures towards the ice-water interface temperature at the freezing point around −1.8 °C. With the thermodynamic model presented in the last section, the sea ice surface temperature and the thermal microwave brightness temperature were simulated using a combination of thermodynamic and microwave emission models (Tonboe et al., 2011).

The simulations indicate that the physical snow-ice interface temperature or alternatively the 6 GHz effective temperature have a good correlation with the effective temperature at the temperature sounding channels near 50 GHz. The physical snow-ice interface temperature is related to the brightness temperature at 6 GHz vertical polarisation as expected. The simulations reveal that the 6 GHz brightness temperature can be related to the snow-ice interface temperature correcting for the temperature dependent penetration depth in saline ice. The penetration is deeper at colder temperatures and shallower at warmer temperatures. This means the 6 GHz T_{eff} is relatively warmer than the snow-ice interface temperature at colder physical temperatures because of deeper penetration, in line with the findings of Ulaby et al. (1986) that the penetration depth increases with decreasing temperatures. Nevertheless it may be possible to derive the snow-ice interface temperature from the 6 GHz brightness temperature. The snow-ice interface temperature estimate may be more easily used in physical modelling than the effective temperature. Hydrodynamic ocean and sea ice models with advanced sea ice modules simulate the snow surface and snow-ice temperatures explicitly.

Remote sensing of sea ice during DAMOCLES

G. Heygster et al.

The simulations with the combined thermodynamic and emission model show that the 6 GHz brightness or effective temperature estimates (Hwang and Barber, 2008) or the snow-ice interface temperature is a closer proxy for the effective temperature near 50 GHz than the snow surface temperature. This is compatible with the value of about 6 cm penetration depth for multiyear ice, as interpolated in Mathew et al. (2008) from Haggerty and Curry (2001).

The snow surface temperature can be measured with infrared radiometers and the effective temperature at 6 GHz can be estimated using the 6 GHz brightness temperature. Because of the large temperature gradient in the snow and the ice and the low heat conduction rate in snow, the snow surface temperature is relatively poorly correlated with both the snow-ice interface temperature and the effective temperatures between 6 and 89 GHz. However, the effective temperatures between 6 GHz and 89 GHz are highly correlated.

4 Snow on sea ice

4.1 Retrieval of snow grain size

Snow on top of the sea ice is little in mass, but strongly influences the albedo of the sea ice, and thus, the local radiative balance, which plays an essential role for the albedo feedback process and ice melting. The albedo of snow does not have a constant value, but depends on the grain size (smaller grains have higher albedo) and the amount of pollution like soot and in fewer cases dust, which both lower albedo significantly. Satellite remote sensing is an important tool for snow cover monitoring, especially over difficult-to-access polar regions.

Within DAMOCLES, a new algorithm for retrieving the Snow Grain Size and Pollution (SGSP) for snow on sea ice and land ice from satellite data has been developed (Zege et al., 2008, 2011). This algorithm is based on the analytical solution for snow reflectance within the asymptotic radiative transfer theory (Zege et al., 1991). The unique

features of the SGSP algorithm are that it does not use any assumptions on snow grain shape in the retrieval process, its results depend only very weakly on the snow grain shape and its regards to the Bidirectional Reflectance Distribution Function (BRDF) of the snow pack. It works at low sun elevations, which are typical for polar regions. Because of the analytical nature of the basic equations used in the algorithm, the SGSP code is fast enough for near-real time applications to large-scale satellite data. The SGSP code includes the new atmospheric correction procedure that accounts the real BRDF of the particular snow pack.

Note that developments of earlier methods for snow remote sensing (Han et al., 1999; Hori et al., 2001; Stamnes et al., 2007) were based on the model of snow as an ensemble of spherical ice particles. In these approaches Mie code was used to calculate snow optical characteristics and some radiative transfer codes were deployed to calculate look up tables (LUT-Mie technique). It seemed that the fact that snow grains in polar snow packs tend to become rounded during the metamorphism process made this concept more trustworthy. But the phase functions of these rounded grains (as of all other particles that are not ideal spheres) drastically differ from those for ideal ice spheres particularly for the scattering angles in the range 70°–130° typical for satellite remote sensing as with MODIS in polar region. This feature cannot be described with the Mie theory (Zege et al., 2011). Within DAMOCLES it was shown that these methods could provide admissible accuracy only when zenith angles of the sun are less than 40°–50°. In polar regions, where the sun position is generally low, the frequently used LUT-Mie technique and the disregard of the real snow BDRF (particular the use of the Lambertian reflectance model) may lead to unacceptable errors in the retrieved values. This is illustrated in the computer simulations of Fig. 4. The comparatively fresh snow that is modeled as a mixture (MIX) of different ice crystals is considered here with grain effective size of 100 µm and a soot load of 1 ppm.

This simulations were performed with the software tool SRS (Snow Remote Sensing), developed under DAMOCLES specifically to study the accuracy of various approaches and retrieval techniques for snow remote sensing. SRS simulates the

bidirectional reflectance from a snow-atmosphere system at the atmosphere top and the signals in the spectral channels of optical satellite instruments. SRS includes the accurate and fast radiative transfer code RAY (Tynes et al., 2001), realistic and changeable atmosphere models with stratification of all components (aerosol, gases) and realistic models of stratified snow. The simulated signals in the spectral channels of MODIS were used for retrieval performed both with SGSP and Mie-LUT codes. The SGSP method provides reasonable accuracy at all possible solar angles while the LUT-Mie retrieval technique fails when snow grains are not spherical at oblique solar angles. This conclusion is of great importance for snow satellite sensing in polar regions where the sun elevation is always low.

The SGSP includes newly developed iterative atmospheric correction procedure that allows for the real snow BDRF and provides a reasonable accuracy of the snow parameters retrieval even at the low sun positions typical for polar regions.

The SGSP algorithm has been extensively and successfully validated (Zege et al., 2011) using computer simulations with SRS code. Detailed comparison with field data obtained during campaigns carried out by Aoki et al. (2007), where the micro-physical snow grain size were measured using a lens and a ruler, was performed as well (Wiebe et al., 2012). The SGSP-retrieved snow grain size complies well with the in-situ measured snow grain size.

The SGSP code with the atmospheric correction procedure is operationally applied in the MODIS processing chain providing MODIS snow product for selected polar regions (see www.iup.uni-bremen.de/seaice/amsr/modis.html). Figure 5 shows an example of the operational retrieval of snow grain size on the Ross ice shelf.

4.2 In situ measurements snow reflectance

For validation of any remote surface sensing observations from satellite, in situ observations are required. These are difficult to obtain in the high Arctic. The in situ component of the Damocles project has helped to fulfil these requirements with a campaign

Title Page

Abstract | Introduction

Conclusions | References

Tables | Figures

|◄ | ►|

◄ | ►

Back | Close

Full Screen / Esc

Printer-friendly Version

Interactive Discussion

of 15 scientists and of 2 weeks total duration to Longyearbyen, Svalbard, and to the schooner Tara drifting with the sea ice (Gascard et al., 2008).

The original plan had been to measure snow the reflectance with a sun photometer CIMEL CE 318 at both places. However, it turned out that the sea ice surface near Tara

5 drifting at the time of the campaign near 88° N was too rough so that snow reflectance measurements were only taken in Longyearbyen. The observation site was the flat top of a 450 m high hill with few radomes for satellite communications at a distance of several hundreds of meters (Fig. 6). The terrain was gently sloping towards 5° W.

The sun photometer CIMEL CE 380 had been equipped with two additional heatings

10 and a thermal insulation (Fig. 6) in order to ensure reliable functioning of the electrical and mechanical drive and the electronics under Arctic conditions. The photometer is able to observe at 8 wavelengths of which 6 were used here, namely 1020, 870, 670, 440, 500, and 340 nm. The channels at 940 nm and 380 nm, strongly influenced by water vapour and calibration problems, respectively, were not used. Three types

15 of radiance measurements were performed, in the sky along the sun principal plane and along sun almucantars, i.e. circles parallel to the horizon at the sun elevation, and on the surface the reflectance in direction towards the sun and perpendicular to it. While the sky measurement sequences are ready programmed in the photometer by the provider, the reflectance measurements were realized by an additional metal mirror

20 placed under an angle of 45° in front of the photometer, deflecting the incoming radiation by 90° from the ground so that the pre-installed sun principal plane observation program could also be used for the surface measurements. The opening angle of the photometer of 1.2° leads at a height of the photometer head of 1.2 m above ground to a footprint of the sensor on ground varying between 1.3 and 7.2 mm if the observing

25 zenith angles varies from 10° to 80°.

The snow reflectance at view nadir angles 0 to 80° was measured on 21 April. Figure 7 and Table 1 show the results from two wavelengths, 1040 and 440 nm. At 440 nm, the reflectance increases from about 0.9 to 1.6 with the view angle towards the sun increasing from 0° to 80°. In the perpendicular direction, the increase is much slower and

Remote sensing of sea ice during DAMOCLES

G. Heygster et al.

Title Page

Abstract | Introduction

Conclusions | References

Tables | Figures

|◄ | ►|

◄ | ►

Back | Close

Full Screen / Esc

Printer-friendly Version

Interactive Discussion

reaches only up to about 1.0. In both directions, several curves have been taken. The observed variability of the reflectance can be explained with the small diameter of the footprint, so that different and independent spots are observed from one photometer run to the next. The reflectance at 1020 nm wavelength shows a similar behaviour, but

5   starts at clearly lower values ($\approx$0.7). The increase in the direction perpendicular to the sun reaches 0.9 at 80° view angle, but values as high as 1.9 towards the sun.

From a Lambertian surface, we would expect a reflectance constant in view angle. In both observing directions we note that surface does not behave Lambertian, but for different reasons: towards the sun, there is an additional broad specular component,

10   which we can interpret as being caused by an orientation distribution of the flat snow crystals on ground with a broad maximum at flat orientation. A purely specular component would have a clear peak at the view angle of the sun zenith angle, i.e. 72°, broadened by the orientation distribution of the snow crystals. However, the maximum reflectance has been observed at 80° view angle. This discrepancy can hardly be ex-

15   plained with the sampling distance of 10° view angle. Rather, it may be explained with the glint theory of Konoshonkin and Borovoi (2011) who showed that the width of the peak increases and the VZA of the reflectance maximum decreases with the maximum tilt angle of the snow flakes.

In the direction perpendicular to the sun, the increase of reflectance can be con-

20   firmed visually and qualitatively explained from Fig. 6: the shadows of small-scale roughness in the snow become less visible at more oblique incidence angles.

The findings of Fig. 7 are qualitatively similar to those of Kokhanvosky and Breon (2012) taken from the satellite sensor PARASOL over snow in Greenland and Antarctica in the sense that they start with similar values at nadir observation and in-

25   crease with view angle (Table 1). However, satellite and ground observations differ in two points: first, the maximum observed nadir view angle is in the satellite observations 60° in direction towards sun, and 50° in the direction perpendicular to the sun, in the Antarctic observations it even only 30°, whereas all Longyearbyen ground observations have been performed up to 80° nadir view angle. Second, and perhaps more important,

Title Page

Abstract | Introduction

Conclusions | References

Tables | Figures

|◄ | ►|

◄ | ►

Back | Close

Full Screen / Esc

Printer-friendly Version

Interactive Discussion

the increase of the reflectance with view angle is in all cases clearly more pronounced in the Longyearbyen observations, and the strong increase of the reflectance beyond 60° in the direction toward the sun is completely missed in the PARASOL observations. On the other hand, the PARASOL observations also cover negative view angles, i.e. in the direction pointing away from the sun, which have not been taken in situ, so that both observations may complement each other when being used for modelling the snow reflectance. Konoshonkin and Borovoi (2011) have developed a theory

The reflectances at the various wavelengths (Fig. 8a) can be used to determine the effective grain size which best fits the reflectance spectrum. This has been done using the forward model of Kokhanovsky et al. (2011), leading to an effective grain size of 0.122 mm. The reflectances obtained from the forward model with this value are also shown in Fig. 8a and b shows the agreement of the underlying reflectance function with the observations, at least in the wavelength range up to 1020 nm.

4.3 Snow albedo

Currently the snow albedo is found using several satellite instruments. Routine visible satellite observations of the polar regions began in 1972 with launch of the first Landsat. The NOAA/AVHRR sensor provides the longest time-series of surface albedo observations currently available. The AVHRR Polar Pathfinder (APP) (Fowler et al., 2000) product is available from the National Snow and Ice Data Center (http://nsidc.org), providing twice daily observations of surface albedo for the Arctic and Antarctic from AVHRR spanning July 1981 to December 2000. The accuracy of this product is estimated to be approximately 6 % (Stroeve et al., 2001). A prototype snow albedo algorithm for the MODIS instrument was developed by Klein and Stroeve (2002). Models of the bidirectional reflectance of snow created using a discrete ordinate radiative transfer (DISORT) model are used to correct for anisotropic scattering effects over non-forested surfaces. Maximum daily differences between the five MODIS broadband albedo retrievals and in situ albedo are 15 %. Daily differences between the "best" MODIS broadband estimate and the measured SURFRAD albedo are 1–8 %. Recently, Liang et al. (2005)

developed an improved snow albedo retrieval algorithm. The most important improvement to the direct retrieval algorithm is that the nonparametric regression method (e.g. neural network) used in the previous studies has been replaced by an explicit multiple linear regression analysis. Another important improvement is that the Lambertian assumption used in the previous study has been replaced with a more explicit snow BRDF model. A key improvement is the inclusion of angular grids that represent reflectance over the entire Sun-viewing angular hemisphere. A linear regression equation is developed for each grid, and thus thousands of linear equations are developed in this algorithm for converting TOA reflectance to surface broadband albedo directly.

The shortcoming of methods described above is the use of an assumption that the snow grains have a spherical shape. Therefore, we have developed an approach, which is based on the model of aspherical snow grains. In particular we have used the following equation for snow reflectance function R (Zege et al., 1991):

$$R = R_0 A^p. \tag{1}$$

Here A is the snow albedo, R_0 is the snow reflection function for the nonabsorbing aspherical grains (pre-calculated values are assumed for fractal snow grains) and $p = K(\mu_0) K(\mu)/R_0$, $K(\mu) = \frac{3}{7}(1 + 2\mu)$, μ is the cosine of the observation zenith angle and μ_0 is the cosine of the solar zenith angle. The atmospheric correction is applied to satellite data for the conversion of satellite – measured reflectance R_{sat} to the value of snow reflectance R. Such an approach was validated using ground measurements (Negi and Kokhanovsky, 2010) and found to be a robust and fast method to derive snow albedo with account for the snow BRDF. We note that Eq. (1) can be used directly to find the snow albedo:

$$A = (R/R_0)^{1/p}. \tag{2}$$

The results of retrievals for Spitzbergen are given in Fig. 9. They are based on MERIS on board ENVISAT.

Remote sensing of sea ice during DAMOCLES

G. Heygster et al.

Title Page

Abstract | Introduction

Conclusions | References

Tables | Figures

|◀ | ▶|

◀ | ▶

Back | Close

Full Screen / Esc

Printer-friendly Version

Interactive Discussion

5 Sea ice drift and deformation

Sea ice dynamics causes transport of fresh water and negative latent heat, and ice dynamics influences the heat transfer between ocean and atmosphere. Within DAMO-CLES, sea ice drift has been investigated with several sensors operating at different horizontal scales: with the scatterometer ASCAT and microwave radiometers, both yielding drift fields at 50–100 km resolution (Sects. 5.1 and 5.4), with the optical sensor AVHRR (Sect. 5.2), and with the Synthetic Aperture Radar ASAR (Sect. 5.3). Finally, conclusions drawn from analysis of sea ice deformation, based on the derivative of the ice motion, are introduced in Sect. 5.5.

The European polar-orbiting satellite Metop-A was launched in October 2006, timely with the sea ice research activities of DAMOCLES and the IPY, as it carries two relevant observing systems, namely the Advanced Scatterometer (ASCAT), and the Advanced Very-High Resolution Radiometer (AVHRR).

5.1 ASCAT and multi-sensor sea ice drift at IFREMER/Cersat

Like SeaWinds/QuikSCAT, the scatterometer ASCAT is primarily designed for wind estimation over ocean. It is a C-band radar (5.3 GHz) like two precursors on the European Research Satellites ERS-1 and ERS-2, respectively, henceforth together denoted as ERS. Like ERS also, the ASCAT observing geometry is based on fan-beam antennas. Over sea ice, the backscatter is related to the surface roughness of ice (at the scale of the wavelength used), which in turn is linked with ice age (Gohin, 1995). In contrast to open water, the backscatter is not a function of the azimuth of the beam but varies strongly with incidence angle. As a consequence, swaths signatures are clearly visible in ASCAT backscatter data, indicating that such data can not be used directly for geophysical interpretation. It is indeed mandatory to construct incidence-adjusted ASCAT backscatter maps for sea ice application. It is noteworthy that the backscatter from SeaWinds/QuikSCAT scatterometer does not require an incidence angle correction because of its conically revolving antennas providing constant incidence angle.

Remote sensing of sea ice during DAMOCLES

G. Heygster et al.

Based on the experience from ERS and NSCAT data, IFREMER has developed algorithms to compute incidence-adjusted backscatter maps normalized to 40° incidence angle. Once corrected, the backscatter values over sea ice can be further interpreted with horizontally homogeneous retrieval algorithms in order to detect geophysical structures which can be compared to those from SeaWinds/QuikSCAT maps. ASCAT offers a complete daily coverage of the Arctic Ocean, although some peripheral regions are not entirely mapped each day (e.g. Baffin Bay).

One application of the ASCAT incidence-adjusted backscatter maps is to estimate sea ice displacement. Although single ice floes can not be detected with the low pixel resolution available with microwave sensors such as ASCAT (typically 10–20 km), the general circulation of sea ice can effectively be mapped on a daily basis. Several motion extraction methods have been tested, based on tracking common features in pairs of sequential satellite images. The most commonly used technique, the Maximum Cross Correlation (MCC), enables only detection of translation displacement (Kamachi, 1989; Ninnis et al., 1986). The main limitation of the MCC is the angular resolution for small drifts: the vector direction in slow motion areas has a larger uncertainty. A correlation is estimated between an array of the backscatter/brightness temperature map in one day and an array of the same size of another map separated in time. In particular, Ezraty et al. (2007) apply this process on the Laplacian field in order to enhance the structures to be tracked. The relative location of the maximum similarity between the arrays of the two original images is the displacement vector. To remove outliers, a threshold minimum correlation coefficient is imposed, and a comparison with the wind pattern is often applied (ECMWF model for Ezraty et al., 2007; NCEP re-analyses for Kwok et al., 1998) since mean sea ice drift is strongly linked with geostrophic winds.

Brightness temperature maps from passive microwave radiometers have been used for sea ice drift estimation since the 1990's. The same method has been applied to scatterometer data, first with 12.5 km pixel resolution one day average Sea-Winds/QuikSCAT backscatter maps and now with ASCAT (same grid resolution). This allows to process every day during winter, 3 and 6 day lag ice drift maps since

1992 with radiometers (SSM/I, AMSR-E) and scatterometers since 1999 with Sea-Winds/QuikSCAT (Ezraty et al., 2007) and ASCAT. The noise level is dominated by sensor ground resolution and pixel size. Advantages and shortcomings of each product depend on pixel sizes, period and magnitude of drift.

5   One recent major improvement of these drift estimation is the combination of two drift fields (QuikSCAT with SSMI and now ASCAT with SSMI): it provides better confidence in the results than each individual one since each drift is inferred from independent measurements. The number of valid drift vectors is increased, in particular for early fall and early spring (more than 20 %), and the merged drift enables discrim-
10 ination of outliers remaining in the individual products (Girard-Ardhuin et al., 2008). A time and space interpolation algorithm has been added to fill the gaps and provide the fullest field as possible, as often requested by the modelling community. The CERSAT/IFREMER time series is ongoing for Arctic long term monitoring with the Metop/ASCAT scatterometer data. Data are easy and free access via the CERSAT por-
15 tal (http://cersat.ifremer.fr). The Merged product QuikSCAT/SSMI has been validated against IABP buoys (Girard-Ardhuin et al., 2008). Characteristic values of products are found in Table 2.

5.2 Sea ice drift from AVHRR observations

For the DAMOCLES project, a Maximum Cross Correlation (MCC) sea ice motion re-
20 trieval algorithm was developed for data from the Metop/AVHRR instrument. The set-up operates on swath data at original spatial resolution (approximately 1 km) of visible (VIS, channel 2) and Thermal InfraRed (TIR, channel 4) data. The VIS data are used during sunlit periods, where the TIR data show poor applicability for feature recognition, as a consequence of low temperature difference between snow/ice and water. The TIR
25 data are thus used during autumn, winter and spring, when leads, ridge zones and thin ice are easily recognised in the data. Characteristic values of the set-up are found in Table 2.

The use of satellite based VIS and TIR measurements for sea ice drift retrievals is limited by the presence of clouds and the applicability is therefore constraint to areas below clear skies. This limitation, in combination with comprehensive filtering for dubious ice displacement vectors, causes large data gaps, especially during the Arctic summer when cloud cover prevails. However, the advantage of using AVHRR data for ice drift monitoring is the daily coverage of the Arctic region with high spatial resolution, providing high precision ice drift estimates. A comparison of this product to high precision GPS buoy positions show that the standard deviation of the 24 h displacement error is around 1 km in both summer and winter (Hwang and Lavergne, 2010).

The AVHRR ice motion product is suited for data assimilation and for tuning of model ice parameters, like sea ice strength, thanks to its fine temporal and spatial resolution, as well as the high product accuracy. The product should also prove useful for validation of modelled sea ice motion. This 24 h ice motion product has subsequently been operationalized and is now available as a test product from the OSISAF web portal as of mid 2011 (http://osisaf.met.no).

5.3 Sea ice drift from ASAR observations

Following the launch of the Radarsat-1 satellite in November 1995, ice drift and deformation applications such as the Radarsat Geophysical Processing System (RGPS) at the Alaskan SAR Facility (ASF) were developed. However, the Radarsat data were only available to the scientific community in very limited numbers, mainly due to the cost of the images. In 2002, ESA launched the Envisat satellite with its Advanced Synthetic Aperture Radar (ASAR) instrument and the data coverage increased tremendously. After the release of the coarse resolution (1000 m) Global Monitoring Mode (GMM) images in 2004, ice feature tracking from these images was developed at the Danish Technical University (DTU). In June 2007, ESA started providing a much improved coverage of the polar regions, now in the finer resolution (150 m) Wide Swath Mode (WSM). Daily coverage of the European sector of the Arctic has been available almost continuously since 2007. The DTU processing scheme was adapted to the higher

resolution WSM scenes, and a dataset of daily ice drift vectors from June 2007 to the present is being continuously updated, now as part of the EU MyOcean project. The individual 150 m resolution data-files are gridded to a polar stereographic projection at 300 m grid spacing, and ice features are tracked on a 10 km grid between each swath of day 1 and each swath of day 2, that are separated in time by between 12 and 36 h (Table 2). The processing provides very accurate ice drift vectors from the coverage area (uncertainty less than 500 m in 24 h). Validation with GPS drift buoys show RMS uncertainties of between 200 m and 600 m for the 12–36 h drift vectors depending somewhat on area and season (Hwang and Lavergne, 2010). This is substantially better than most other ice drift products, but the drawback is that the coverage is generally limited to the area of the Arctic Ocean between 90° W and 90° E. In addition the SAR coverage only extends to approximately 87° N.

5.4 Multi-sensor ice drift analysis at the EUMETSAT OSI SAF

All ice drift products described above are based on the Maximum Cross Correlation (MCC) algorithm. However, the MCC exhibit strong weaknesses when the length of the displacement is short with respect to the pixel size. For example, displacements that are less than half an image pixel in length cannot be observed and are measured as zero-drift. For the same reason, the angular resolution of the motion vector field is poor for short displacement lengths. This noise is often referred to as the quantization noise, or tracking error. While this does not restrict the usefulness for motion tracking from high-resolution images (e.g. SAR or AVHRR, see above), the quantization noise is largely apparent in MCC-based motion vector fields from low-resolution images acquired by passive microwave instruments such as SSM/I, and AMSR-E and scatterometers such as QuikSCAT/SeaWinds and ASCAT (Sect. 5.1).

An alternative motion tracking method was thus developed during the DAMOCLES project. The Continuous Maximum Cross-Correlation (CMCC, Lavergne et al., 2010) is strongly linked to the MCC, but uses a continuous optimization step for finding the motion vector that maximizes the correlation metric. As a result, the quantization

noise is removed, and the motion field obtained from the low-resolution images is spatially smooth and does not exhibit the MCC artefacts such as zero-length vectors and poor angular resolution. Particularly, the deformation metrics such as the convergence/divergence are more realistic from a field processed by the CMCC than by the MCC (see Sect. 5.5).

The CMCC was successfully applied to ice motion tracking from AMSR-E (37 GHz), SSM/I (85 GHz), and ASCAT daily images (12.5 km grid spacing). Validation against GPS buoys document un-biased and accurate estimates, with standard deviation of the error in x and y displacement ranging from 2.5 km to 4.5 km after 48 h drift, depending on the instrument used.

The ice drift algorithms of Lavergne et al. (2010) were implemented in the operational processing chain of the EUMETSAT OSI SAF in late 2009. Daily products (OSI-405, both single- and multi-sensor, Table 2) are available from the OSI SAF web site (http://osisaf.met.no) for use in sea ice monitoring and data assimilation by coupled ocean and ice models (Lavergne and Eastwood, 2010).

5.5 Sea ice deformation

Sea ice drift and deformation cause leads and faulting in the sea ice cover with subsequent exposure of ocean to the atmosphere, increasing the transport of heat and humidity from the ocean to the atmosphere by one to two orders of magnitude. The degree of deformation is depending on the main forcing parameters, wind and ocean current, and on the strength of the ice sheet.

It is documented that thin ice deforms easier than thick ice (Kwok, 2006; Rampal et al., 2009; Stern and Lindsay, 2009). Ice deformation characteristics is therefore a proxy for ice thickness and thus an indicator of the state of the Arctic sea ice, provided that the wind and ocean forcing is relatively constant. It is therefore reasonable to assume that the graduate thinning of the Arctic sea ice in particular since 2002, as documented by e.g. Kwok et al. (2009), is reflected in the deformation data. This study, and studies by e.g. Marsan et al. (2004) and Stern and Lindsay (2009) show that sea

ice deformation estimates can be derived from ice drift fields like those described in the sections above, thus making it possible to produce large scale sea ice deformation data sets for numerical analysis.

An ice drift data set, based on the full time series of AMSR-E data (from 2002 to present) was analysed for changes in Arctic sea ice deformation. The AMSR-E ice drift data set is produced using the CMCC methodology also applied to the low resolution OSISAF ice drift product (OSI-405), mentioned in Sect. 5.4. Ice deformation is calculated for the Northern Hemisphere using only the highest quality drift vectors, with directional errors of less than 3 km for 48 h drift. The divergence is calculated from a standard mathematical term for area change of a deformed square (Quadrilateral, 2010; Dybkjaer, 2010). The uniqueness of this ice drift and deformation data set lies in the combination of high precision, daily full-Arctic coverage, input data consistency through the single sensor status and the fact that it covers the most dramatic period of recent Arctic sea ice cover history, namely 2002 to present time.

A plot of mean Arctic sea ice deformation through a 10 day period, based on the AMSR-E data set, is shown in Fig. 10. The general pattern is a broad convergence zone (dark colours) from the low part of the Beaufort Sea to the East Siberian Sea and diverging areas (light colours) in the central Beaufort Sea and Chukchi Sea. This is a typical deformation pattern caused by high pressure conditions over the Beaufort Sea.

Monthly sea ice deformation data for the Northern Hemisphere, since 2002, are shown in Fig. 11, as mean values of accumulated divergence and convergence. The most conspicuous feature here are the increased deformation values during early winter month, after the winter of 2007/2008, followed by less high deformation values in the past 2 winters. This is in agreement with the replacement of vast areas of multi year ice with first year ice after the summer of 2007 and a partly recovery of ice older than 1 yr the following years. This ice age redistribution is clearly evident from the Arctic ice age distribution estimated by NSIDC (201104).

A surface wind deformation index, calculated from 10 m wind fields from the operational global model at ECMWF, is also plotted in Fig. 11. This index and the

corresponding mean wind-speed values in Fig. 12 are included to make plausible that the shift in ice deformation pattern after 2007 is not associated with changing atmospheric circulation, as neither the surface wind divergence nor the wind-speeds show trends since 2002. However, deformation pattern on a full Arctic scale, cover for large
5 spatial variability, which at present is under investigation and will be published later.

Where the mean Arctic sea ice deformation data revealed no smooth trend following the general thinning of Arctic sea ice, changes the wind drag on sea ice show a clear increasing trend since 2002. This is clear in Fig. 12 where corresponding ice-speed/wind-speed ratios for five winter months since 2002/2003, are plotted. The best
10 fitted line to the data between the winters of 2002/2003 and 2009/2010 gives an increased in wind drag ration of approximately 25 % since 2002/2003. This is a large increase in wind drag, considering that the mean wind-speed and divergence in the period seems constant during the period.

6 Sea ice thickness

15 Satellite altimeter data can provide extensive spatial and temporal measurements of sea ice thickness through converting ice freeboard measurements to thickness by assuming hydrostatic equilibrium (Laxon et al., 2003). Analysis of ERS and Envisat radar-altimeter (RA) data from 1992 to present has resulted in a unique data set on ice thickness south of 81.5° N (Giles et al., 2008). These ERS/Envisat sea-ice thick-
20 ness time series will be extended by CryoSat-2, which was launched in April 2010 and carries a RA that operates in Synthetic Aperture Radar mode over sea ice, providing freeboard measurements with 250 m resolution along the satellite track (ESA, 2003).

Under the assumption of the hydrostatic equilibrium the equation for calculation of sea ice thickness H_i from its freeboard (F_i), measured by RA, is given by:

25 $$H_i = \frac{\rho_w}{(\rho_w - \rho_i)} F_i + \frac{\rho_{sn}}{(\rho_w - \rho_i)} H_{sn} \tag{3}$$

where ρ_i, ρ_w, and ρ_{sn} are sea ice, water and snow densities, H_{sn} is snow thickness. Laxon et al. (2003) and Giles et al. (2008) used this approach to calculate ice thickness in a basin wide scale with the prescribed values of seawater and sea ice densities and snow loading climatology from (Warren et al., 1999).

The main objective of our studies, conducted in the frames of the DAMOCLES project, consisted of studying the relation between ice freeboard and ice thickness using extensive in-situ sea ice measurements from the airborne Sever expeditions. The Sever expeditions provide one of the most extensive data sets of sea ice and snow parameters collected in 1928, 1937, 1941, 1948–1952, and 1954–1993. The measurements were conducted mostly from mid March to early May, when landing on ice floes was possible. The total data set, including 3771 landings, was obtained from the World Data Center for Glaciology/National Snow and Ice Data Center (NSIDC), Boulder, Colorado (National Snow and Ice Data Center, 2004). In this study data from 689 landings in 1980–1982, 1984–1986 and 1988, where freeboard measurements were included, have been analyzed. This subset spans the entire Eurasian Russian Arctic, where first-year ice is prevalent.

Data from the Sever expeditions show that in spring median snow depth on level first-year ice is 0.05 m with the uncertainty of 0.05 m. It is substantially less than that on multiyear ice in the Central Arctic, where in May it amounts to 0.35 ± 0.06 m (Warren et al., 1999). Several other studies support this conclusion to some degree (Yakovlev, 1960; Nazintsev, 1971; Buzuev et al., 1979; Romanov, 1995; Kwok et al., 2009). Romanov (1995) reports snow depth values of 0.05 and 0.08 m for ice thicknesses less or more than 1.60 m, respectively, and that the thinnest snow cover on first-year ice is in the Canadian and Alaskan regions, and the deepest in the Greenland region. According to Buzuev et al. (1979) snow depth on multiyear ice is 50 % more than that on level first-year ice. Estimates by Kwok et al. (2009) show that snow depth on first-year ice amounts to 46 and 66 % of that on multiyear ice in autumn and winter, respectively. Nazintsev (1971) found that in spring snow depth on level drifting floes in the Kara Sea varies from 5 to 13 cm, which is approximately three times less than that on fast ice. In

Title Page

Abstract | Introduction

Conclusions | References

Tables | Figures

◄ | ►

◄ | ►

Back | Close

Full Screen / Esc

Printer-friendly Version

Interactive Discussion

Fram Strait the average snow layer on both first-year and multiyear ice is 19 cm thick in spring, and it varies greatly due to its redistribution by wind on an uneven surface. In the Barents Sea the snow depth is 13 cm on average and varies less (Forsstrom et al., 2011).

Several studies support the notion that snow densities on both first-year and multiyear ice are rather similar. The average snow density on first-year ice, calculated from the Sever data, is 324 ± 50 kg m^{-3}. Nazintsev (1971) reports snow density values in the range of 0.30–0.34 kg m^{-3} in the Kara Sea. The density of snow on multiyear ice in March–May is in the range of 310–320 kg m^{-3} (Romanov, 1995; Warren et al., 1999), and is 340 kg m^{-3}, as estimated from measurements during SHEBA (Sturm et al., 2002). The difference in snow properties between multiyear and first-year ice is therefore related to snow depth, not to snow density.

The density of first-year ice was calculated for each of the 689 landings in Sever data by substituting H_i, F_i, and H_{sn} measurements, the mean calculated snow density (324 kg m^{-3}), and water density value of 1025 kg m^{-3} to the Eq. (2) leading to

$$\rho_i = \rho_w - \frac{\rho_w F_i + \rho_{sn} H_{sn}}{H_i}. \tag{4}$$

The mean ice density for first-year ice from the Sever data is 917 ± 36 kg m^{-3}. Analysis of publications shows that density of multiyear ice changes in wide range (Alexandrov et al., 2010). Generally there are lower values for multiyear ice compared to first-year ice above the waterline, which closely corresponds to the occurrence of air-filled pores in its freeboard layer (Timco and Frederking, 1996).

Our studies revealed that snow loading and ice density can be substantially different for first-year and multiyear ice. Therefore an approach to ice thickness calculation from RA data should be based on separate calculation of ice thickness for these ice types. Areas of open water, new and young ice, first-year ice and multiyear ice can be delineated from composite ice charts, weekly issued by Arctic and Antarctic Research Institute (Fig. 13). Thickness of level first-year ice in the Eurasian Arctic in the period

March–May can be calculated using linear regression Eq. (3), derived from the Sever data:

$$H_i = 8.13\, F_i + 0.37. \tag{5}$$

However, taking into consideration that snow climatology by Warren et al. (1999) does not cover first-year ice, ice thickness can be calculated during the whole winter, assuming that snow loading on the ice does not substantially change. In Fram Strait and in the Barents Sea ice thickness can be calculated using the empirical relations by (Vinje and Finnekåsa, 1986) or (Forsstrom et al., 2011). It is also possible to use hydrostatic equilibrium equation and to construct daily fields of snow depth using available climatology and snowfall from ECMWF meteorological products for partitioning the total freeboard into its snow and ice components, as described by Kwok and Cunningham (2008). Another possibility is to use AMSR-E snow depth averaged product (Kurtz et al., 2009; Cavalieri et al., 2010). The accuracy of these snow depth estimates should be compared and validated. In the areas of thin ice it is more difficult to derive ice thickness from RA data. It is expected that ice thickness in large areas of young ice will be determined using passive microwave radiometer data from Soil Moisture and Ocean Salinity (SMOS) satellite, which operate at 1.4 GHz frequency (Heygster et al., 2009; Kaleschke et al., 2010).

Using Sever data the accuracy of the ice thickness retrieval has been calculated from the estimated variability in ice and snow parameters and error of ice freeboard measurements. It is found that uncertainties of ice density and freeboard are the major sources of error in ice thickness calculation. For first-year ice, retrieval of ≈1.0 m (2.0 m) thickness has an uncertainty of 46 % (37 %), assuming that the freeboard error is ± 0.03. If the freeboard error can be reduced to 0.01 m by averaging measurements from CryoSat-2, the error in thickness retrieval is reduced to about 32 % for a 1.0 m thick first-year floe. The remaining error is dominated by uncertainty in ice density. These results are applicable for first-year ice in the Eurasian Arctic. In Fram Strait (Forsstrom et al., 2011) found much larger error of 37 cm for RA due to snow loading uncertainty.

Thickness of multiyear ice can be calculated from the hydrostatic equilibrium equation with prescribed value of ice density, snow loading climatology from Warren et al. (1999) or daily fields of snow depth. The major problem here is the correct estimate of multiyear ice density. Provision of improved ice density data is therefore necessary for accurate retrieval of ice thickness from CryoSat-2 data.

7 Conclusions

In this review the main achievements of the DAMOCLES project in the field of remote sensing of sea ice have been presented. The backbone of sea ice remote sensing are passive microwave sensors like SSM/I, SSM/IS and AMSR-E. The radiance emitted the surface is determined by the product of physical temperature and emissivity. The main limiting factor in sea ice retrieval is the uncertainty in the emissivity, which is much higher and much more variable compared to open water. In order to better know the sea ice emissivity, it has been determined including correlation values between the different channels (Figs. 1 and 2). Applying the results in the framework of an integrated retrieval of surface and atmospheric parameters shows that for a successful procedure it is necessary to better predict the emissivities, e.g. based on the meteorological history.

As a first step towards this goal, in Sect. 1.2 the combination of a thermodynamic sea ice evolution model and a microwave emissivity model has been presented. Application of the model in the numerical weather prediction model HIRLAM shows that tropospheric temperature sounding over sea ice, currently not done operationally, is feasible.

Snow on sea ice acts as a thermal insulator and increases the albedo, which in turn is mainly controlled by the snow grain size (SGS). A method to retrieve the SGS has been developed, with the specific new features not to assume spherical snow crystals (as is usually done) and to work up to sun incidence angles up to over 70°, a common condition in the polar regions (Figs. 4 and 5).

Moreover, a retrieval procedure for the broadband albedo without assuming spherical particles as usual before was established and applied to observations over Greenland (Fig. 9). The consequences of modifying accordingly atmospheric and ocean circulation models are currently investigated in a subsequent project.

Several methods, based on Maximum Cross Correlation (MCC) to retrieve the sea ice drift from the ENVISAT sensors ASCAT, AVHRR and ASAR and a sensor combination have been improved. Typically the drift products have a lower horizontal resolution than the underlying sensor data (Table 1), but as digital derivatives they still tend to enhance noise present in the basic data. An improved Continuous MCC (CMCC) method, originally developed for the multi-sensor drift product, delivers drift fields smooth enough to determine the sea ice deformation (Sect. 5.5).

It is remarkable how the concerted effort of the scientific community during DAMO-CLES to deploy, retrieve and share data from the ice surface directly benefited this validation work. Sea ice position data from the International Arctic Buoy Programme (IABP) and from drifting stations NP-35, NP-36, Tara, and 16 CALIB buoys deployed during the Tara expedition entered the study. The drift results were assimilated into the NAOSIMDAS model study and were used during the Sea Ice Outlook 2009 campaign. The ice drift production and further development is ensured through national projects and the Continuous Development and Operations Phases of EUMETSATs OSI SAF, where ice deformation is analysed for climate monitoring (Lavergne et al., 2010).

Large-scale remote sensing of sea ice thickness, done with freeboard observations from altimeters, is still a challenge. The analysis of the in-situ measurements of sea ice and snow parameters, collected in the airborne Sever expeditions between 1928 and 1993, has shown that currently the most important contributions to the thickness error are the uncertainties in ice density and measurements of freeboard. If uncertainty of ice freeboard can be reduced for a typical first-year ice slab of 1 m thickness from 3 cm to 1 cm, as we can expect from the CryoSat-2 observations, the thickness error will reduces from 46 % to 32 %, and the remaining error stems mainly from the uncertainty in the ice density.

References

Alexandrov, V., Sandven, S., Wahlin, J., and Johannessen, O. M.: The relation between sea ice thickness and freeboard in the Arctic, The Cryosphere, 4, 373–380, doi:10.5194/tc-4-373-2010, 2010.

Andersen, S., Tonboe, R., Kaleschke, L., and Heygster, G.: Intercomparison of passive microwave sea ice concentration retrievals over the high-concentration Arctic sea ice, J. Geophys. Res., 112, C08004, doi:10.1029/2006JC003543, 2007.

Aoki, T., Hori, M., Motoyoshi, H., Tanikawa, T., Hachikubo, A., Sugiura, K., Yasunari, T. J., Storvold, R., Eide, H. A., Stamnes, K., Li, W., Nieke, J., Nakajima, Y., and Takahashi, F.: ADEOS-II/GLI snow/ice products – part II: Validation results using GLI and MODIS data, Remote Sens. Environ., 111, 274–290, 2007.

Buzuev, A. Y., Romanov, I. P., and Fedyakov, V. E.: Variability of snow distribution on the ice in the Arctic Ocean, Meteorology and Hydrology, 9, 76–85, 1979 (in Russian).

Cavalieri, D. J., Markus, T., Ivanoff, A., Miller, J., Sturm, M., Maslanik, J. A., Heinrichs, J. F., Gasievski, A. J., Leuschen, C., Krabill, W. B., Sonntag, J. G., and Brucker, L.: An assessment of the AMSR-E snow depth sea ice algorithm using the March 2006 Arctic field campaign aircraft measurements, American Geophysical Union, Fall Meeting 2010, abstract #C41A-0500, 2010.

Divergence, Wolfram Mathworld: 201005, available at: http://mathworld.wolfram.com/Divergence.html, last access: December 2011.

Dybkjaer, G.: Velocity and deformation fields from Medium and Low resolved – Passive Microwave and IR AVHRR data, DAMOCLES Deliverable Report D1.2-03d, 2010.

ESA: CryoSat Science Report, ESA SP-1272, 56 pp., 2003.

Ezraty, R., Girard-Ardhuin, F., and Piollé, J. F.: Sea-ice drift in the Central Arctic estimated

Remote sensing of sea ice during DAMOCLES

G. Heygster et al.

Title Page

Abstract	Introduction
Conclusions	References
Tables	Figures

◀ | ▶

◀ | ▶

Back | Close

Full Screen / Esc

Printer-friendly Version

Interactive Discussion

from SeaWinds/QuikSCAT backscatter maps. User's Manual, Version 2.2, available at: http://cersat.ifremer.fr/, February 2007.

Forsstrom, S., Gerland, S., and Pedersen, C. A: Thickness and density of snow-covered sea ice and hydrostatic equilibrium assumption from in situ measurements in Fram Strait, Barents Sea and the Svalbard coast, Ann. Glaciol., 52, 261–270, 2011.

Fowler, C., Maslanik, J., Haran, T., Scambos, T., Key, J., and Emery, W.: AVHRR Polar Pathfinder Twice-daily 5 km EASE-Grid Composites V003, Boulder, Colorado USA: National Snow and Ice Data Center, Digital media, 2000, updated 2007.

Gascard, J.-C., Festy, J., le Goff, H., Weber, M., Bruemmer, B., Offermann, M., Doble, M., Wadhams, P., Forsberg, R., Hanson, S., Skourup, H., Gerland, S., Nicolaus, M., Metaxian, J.-P., Grangeon, J., Haapala, J., Rinne, E., Haas, C., Heygster, G., Jakobson, E., Palo, T., Wilkinson, J., Kaleschke, L., Claffey, K., Elder, B., and Bottenheim, J.: Exploring Arctic Transpolar Drift During Dramatic Sea Ice Retreat, Eos T. Am. Geophys. Un., 89, 21–28, 2008.

Giles, K. A., Laxon, S. W., and Ridout, A. L.: Circumpolar thinning of Arctic sea ice following the 2007 record ice extent minimum, Geophys. Res. Lett., 35, L22502, doi:10.1029/2008GL035710, 2008.

Girard-Ardhuin, F., Ezraty, R., Croize-Fillon, D., and Piollé, J. F.: Sea-ice drift in the Central Arctic combining QuikSCAT and SSM/I sea ice drift data. User's Manual, Version 3.0., available at: http://cersat.ifremer.fr/, April 2008.

Gohin, F.: Some active and passive microwave signatures of Antarctic sea ice from mid-winter to spring 1991, Int. J. Remote Sensing, 16, 2031–2054, 1995.

Haggerty, H. A. and Curry, J. A.: Variability of sea ice emissivity estimated from airborne passive microwave measurements during FIRE SHEBA, J. Geophys. Res., 106, 15265–15277, 2001.

Han, W., Stamnes, K., and Lubin, D.: Remote sensing of surface and cloud properties in the Arctic from NOAA AVHRR measurements, J. Appl. Meteorol., 38, 989–1012, 1999.

Hansen, J. and Nazarenko, L.: Soot climate forcing via snow and ice albedos, P. Natl. Acad. Sci., 101, 423–428, doi:10.1073/pnas.2237157100, 2004.

Heygster, G., Hendricks, S., Kaleschke, L., Maas, N., Mills, P., Stammer, D., Tonboe, R. T., and Haas, C.: L-band radiometry for sea ice applications, Final report for ESA ESTEC Contract 21130/08/NL/EL, Institute of Environmental Physics, University of Bremen, 2009.

Hori, M., Aoki, T., Stamnes, K., Chen, B., and Li, W.: Preliminary validation of the GLI algorithms

with M Li W., K. Stamnes, B. Chen, and Xiaozhen Xiong, 2001. Snow grain size retrieved from near-infrared radiances at multiple wavelengths, Geophys. Res. Lett., 28, 1699–1702, 2001.

Hwang, B. J. and Barber, D. G.: On the impact of ice emissivity on the sea ice temperature retrieval using passive microwave radiance data, IEEE Geosci. Remote S., 6, 448–452, 2008.

Hwang, P. and Lavergne, T.: Validation and Comparison of OSI SAF Low and Medium Resolution and IFREMER/Cersat Sea ice drift products. Associated and Visiting Scientist Activity Report. SAF/OSI/CDOP/met.no/SCI/RP/151 – Ocean and Sea Ice Satellite Application Facility, available at: http://osisaf.met.no/docs/OSISAF_IntercomparisonIceDriftProducts_V1p2.pdf, 2010.

Kaleschke, L., Maaß, N., Haas, C., Hendricks, S., Heygster, G., and Tonboe, R. T.: A sea-ice thickness retrieval model for 1.4 GHz radiometry and application to airborne measurements over low salinity sea-ice, The Cryosphere, 4, 583–592, doi:10.5194/tc-4-583-2010, 2010.

Kamachi, M: Advective surface velocities derived from sequential images for rotational flow field: limitations and applications of Maximum Cross Correlation method with rotational registration, J. Geophys. Res., 94, 18227–18233, 1989.

Klein, A. G. and Stroeve, J.: Development and validation of a snow albedo algorithm for the MODIS instrument, Ann. Glaciol., 34, 45–52, 2002.

Kokhanovsky, A. and Breon, F.-M.: A reflectance model for snow and its validation using PARASOL multi-angular and multi-spectral observations, IEEE T. Geosci. Remote, in press, 2012.

Konoshonkin, A. and Borovoi, A.: Glints from cirrus clouds, snow blankets, and sea surfaces, Atti della Accademia Peloritana dei Pericolanti, 89, Suppl. 1, C1S8901XXX, 2011.

Kurtz, N. T., Markus, T., Cavalieri, D. J., Sparling, L. C., Krabill, W. B., Gasievski, A. J., and Sonntag, J. G.: Estimation of sea ice thickness distributions through the combination of snow depth and satellite laser altimeter data, J. Geophys. Res., 114, C10007, doi:10.1029/2009JC005292, 2009.

Kwok, R.: Contrasts in the sea ice deformation and production in the Arctic seasonal and perennial ice zones, J. Geophys. Res., 111, C11S22, doi:10.1029/2005JC003246, 2006.

Kwok, R. and Cunningham, G. F.: ICESat over Arctic sea ice: Estimation of snow depth and ice thickness, J. Geophys. Res., 113, C08010, doi:10.1029/2008JC004753, 2008.

Kwok, R., Schweiger, A., Rothrock, D. A., Pang, S., and Kottmeier, C.: Sea ice motion from satellite passive microwave imagery assessed with ERS SAR and buoy motions, J. Geophys. Res., 103, 8191–8214, 1998.

Remote sensing of sea ice during DAMOCLES

G. Heygster et al.

Title Page

Abstract	Introduction
Conclusions	References
Tables	Figures

|◀ | ▶|

◀ | ▶

Back | Close

Full Screen / Esc

Printer-friendly Version

Interactive Discussion

Kwok, R., Cunningham, G. F., Wensnahan, M., Rigor, I., Zwally, H. J., and Yi, D.: Thinning and volume loss of the Arctic Ocean sea ice cover: 2003–2008, J. Geophys. Res., 114, C07005, doi:10.1029/2009JC005312, 2009.

Lavergne, T. and Eastwood, S.: Low resolution sea ice drift Product User's Manual – v1.4. Technical Report SAF/OSI/CDOP/met.no/TEC/MA/128, EUMETSAT OSI SAF – Ocean and Sea Ice Sattelite Application Facility, 2010.

Lavergne, T., Eastwood, S., Teffah, Z., Schyberg, H., and Breivik, L.-A.: Sea ice motion from low resolution satellite sensors: an alternative method and its validation in the Arctic, J. Geophys. Res.-Oceans, 115, C10032, doi:10.1029/2009JC005958, 2010.

Laxon, S. W., Peacock, N., and Smith, D.: High interannual variability of sea ice thickness in the Arctic region, Nature, 425, 947–949, 2003.

Liang, S. L., Stroeve, J., and Box, J. E.: Mapping daily snow/ice shortwave broadband albedo from Moderate Resolution Imaging Spectroradiometer (MODIS): The improved direct retrieval algorithm and validation with Greenland in situ measurements, J. Geophys. Res., 110, D10109, doi:10.1029/2004JD005493, 2005.

Mätzler, C., Rosenkranz, P. W., Battaglia, A., and Wigneron, J. P. (Eds.): Thermal Microwave Radiation – Applications for Remote Sensing, IEE Electromagnetic Wave Series, London, UK, 2006.

Malinka, A. V. and Zege, E. P.: Fraunhofer diffraction by arbitrary-shaped obstacles, JOSA A, 26, 1762–1766, doi:10.1364/JOSAA.26.001762, 2009.

Marsan, D., Stern, H., Lindsay, R., and Weiss, J.: Scale Dependence and Localization of Deformation of Arctic Sea Ice, Phys. Rev. Lett., 93, p. 178501, 2004.

Mathew, N., Heygster, G., Melsheimer, C., and Kaleschke, L.: Surface emissivity of polar regions at AMSU window frequencies, IEEE T. Geosci. Remote, 46, 2298–2306, doi:10.1109/TGRS.2008.916630, 2008.

Mathew, N., Heygster, G., and Melsheimer, C.: Surface emissivity of the Arctic sea ice at AMSR-E frequencies, IEEE T. Geosci. Remote, 47, 4115–4124, doi:10.1109/TGRS.2009.2023667, 2009.

Maykut, G. A.: The surface heat and mass balance, in: The geophysics of sea ice, edited by: Untersteiner, N., 395–464, NATO ASI Series, Plenum Press, New York and London, 1986.

Melsheimer, C., Heygster, G., Mathew, N., and Toudal Pedersen, L.: Retrieval of Sea Ice Emissivity and Integrated Retrieval of Surface and Atmospheric Parameters over the Arctic from AMSR-E data, J. Remote Sens. Soc. Japan, 29, 236–241, 2009.

Remote sensing of sea ice during DAMOCLES

G. Heygster et al.

Title Page

Abstract	Introduction
Conclusions	References
Tables	Figures

◄◄　　►►

◄　　►

Back　　Close

Full Screen / Esc

Printer-friendly Version

Interactive Discussion

National Snow and Ice data Center: Morphometric characteristics of ice and snow in the Arctic Basin: aircraft landing observations from the Former Soviet Union, 1928–1989, compiled by: Romanov, I. P., Boulder, CO: National Snow and Ice Data Center, Digital media, 2004.

Nazintsev, Y. L.: About snow accumulation on sea ice of the Kara sea. Proceedings of the AARI, 303, 185–190, 1971 (in Russian).

Negi, H. S. and Kokhanovsky, A.: Retrieval of snow albedo and grain size using reflectance measurements in Himalayan basin, The Cryosphere, 5, 203–217, doi:10.5194/tc-5-203-2011, 2011.

Ninnis, R. M., Emery, W. J., and Collins, M. J.: Automated extraction of pack ice motion from Advanced Very High Resolution Radiometer imagery, J. Geophys. Res., 91, 10725–10734, 1986.

NSIDC, 201104: available at: http://nsidc.org/arcticseaicenews/2011/040511.html, 2011.

Rampal, P., Weiss, J., and Marsan, D: Positive trend in the mean speed and deformation rate of Arctic sea ice, 1979–2007, J. Geophys. Res., 114, C05013, doi:10.1029/2008JC005066, 2009.

Rodgers, C. D.: Inverse Methods for Atmospheric Sounding – Theory and Practise, 2 of Series on Atmospheric, Oceanic and Planetary Physics, World Scientific, ISBN 981-02-2740-X, 2000.

Romanov, I. P.: Atlas of ice and snow of the Arctic Basin and Siberian Shelf seas, Backbone Publishing Company, 1995.

Schyberg, H. and Tveter, F. T.: Report on microwave ice surface emission modelling using NWP model data. DAMOCLES deliverable report D1.2-02.f, 3 April, 2009.

Schyberg, H. and Tveter, F. T.: Improved assimilation method in NWP and impact on forecast quality in the Arctic, DAMOCLES deliverable report D4.3-09, 13 June 2010.

Seidel, K. and Martinec, J.: Remote Sensing in Snow Hydrology: Runoff Modelling, Effect of Climate Change, Chichester: Springer-Praxis, 2004.

Serreze, M. C., Barrett, A. P., Stroeve, J. C., Kindig, D. N., and Holland, M. M.: The emergence of surface-based Arctic amplification, The Cryosphere, 3, 11–19, doi:10.5194/tc-3-11-2009, 2009.

Shalina, E. V. and Johannessen, O. M.: Multi year sea ice concentration mapping using passive and active microwave satellite data, IEEE Xplore, 1–4, doi:10.1109/MICRAD.2008.4579513, ISBN: 978-1-4244-1986-9, 2008.

Stamnes, K., Li, W., Eide, H., Aoki, T., Hori, M., and Storvold, R.: ADEOS-II/GLI Snow/Ice

Title Page

Abstract | Introduction

Conclusions | References

Tables | Figures

◄ | ►

◄ | ►

Back | Close

Full Screen / Esc

Printer-friendly Version

Interactive Discussion

Products – Part I: Scientific Basis, Remote Sensing of the Cryosphere, 111, 258–273, 2007.

Stern, H. L. and Lindsay, W.: Spatial scaling of Arctic sea ice deformation, J. Geophys. Res., 114, C10017, doi:10.1029/2009JC005380, 2009.

Stroeve, J., Box, J., Fowler, C., Haran, T., and Key, J.: Intercomparison between in situ and AVHRR Polar Pathfinder-derived Surface Albedo over Greenland, Remote Sens. Environ., 75, 360–374, 2001.

Sturm, M., Holmgren, J., and Perovich, D. K.: Winter snow cover on the sea ice of the Arctic Ocean (SHEBA): Temporal evolution and spatial variability, J. Geophys. Res., 107, 8047, doi:10.1029/2000JC000400, 2002.

Timco, G. W. and Frederking, R. M. W.: A review of sea ice density, Cold Reg. Sci. Technol., 24, 1–6, 1996.

Tonboe, R. T.: The simulated sea ice thermal microwave emission at window and sounding frequencies, Tellus, 62, 333–344, doi:10.1111/j.1600-0870.2010.00434.x, 2010.

Tonboe, R. T. and Schyberg, H.: Algorithm theoretical basis document for the OSI SAF 50 GHz sea ice emissivity model, OSI-404, EUMETSAT OSI SAF report, 22, 2011.

Tonboe, R. T., Dybkjær, G., and Høyer, J. L.: Simulations of the snow covered sea ice surface temperature and microwave effective temperature, Tellus A, 63, 1028–1037, 2011.

Tynes, H., Kattawar, G. W., Zege, E. P., Katsev, I. L., Prikhach, A. S., and Chaikovskaya, L. I.: Monte Carlo and multi-component approximation methods for vector radiative transfer by use of effective Mueller matrix calculations, Appl. Optics, 40, 400–412, 2001.

Ulaby, F. T, Moore, R. K., and Fung, A. K.: Microwave remote sensing. Active an passive. Volume III From Theory to Applications, Artech House, Norwood, MA, USA, 1986.

Vinje, T. and Finnekåsa, Ø.: The ice transport through the Fram Strait, Skrifter Nr. 186, Norsk Polarinstitutt, 39 pp., 1986.

Warren, S. G., Rigor, I. G., Untersteiner, N., Radionov, V. F., Bryazgin, N. N., Aleksandrov, Y. I., and Colony, R.: Snow depth on Arctic Sea Ice, J. Climate, 12, 1814–1829, 1999.

Wentz, F. J. and Meissner, T.: AMSR Ocean Algorithm, Algorithm Theoretical Basis Document (ATBD), version 2, Remote Sensing Systems, California, US, 2 November, 2002

Wiebe, H., Heygster, G., and Zege, E. P.: The snow grain size retrieval SGSP from optical satellite data: Validation with ground truth data and detection of snowfall events, submitted to RSE, 2012.

Wiesmann, A. and Mätzler, C.: Microwave emission model of layered snowpacks, Remote Sens. Environ., 70, 307–316, 1999.

Yakovlev, G. N.: Snow cover on drifting ice in the central Arctic, Problems of the Arctic and Antarctic, 3, 65–76, 1960 (in Russian).

Zege, E. P., Ivanov, A. P., and Katsev, I. L.: Image Transfer through a Scattering Medium, Springer-Verlag, Heidelberg, 1991.

Zege, E., Katsev, I., Malinka, A., Prikhach, A., and Polonsky, I.: New algorithm to retrieve the effective snow grain size and pollution amount from satellite data, Ann. Glaciol., 49, 139–144, 2008.

Zege, E. P., Katsev, I. L., Malinka, A. V., Prikhach, A., Heygster, G., and Wiebe, H.: Algorithm of the effective snow grain size and pollution amount retrieval from satellite data, Remote Sens. Environ., 115, 2674–2685, 2011.

Remote sensing of sea ice during DAMOCLES

G. Heygster et al.

Title Page

Abstract | Introduction

Conclusions | References

Tables | Figures

◄ | ►

◄ | ►

Back | Close

Full Screen / Esc

Printer-friendly Version

Interactive Discussion

Table 1. Comparison of reflectances taken in situ at Longyearbyen (this paper), and from space by PARASOL over Greenland and Antarctica (Kokhanvosky and Breon, 2011).

	Direction towards sun			Direction perpendicular sun		
	0°	60°	80°	0°	50°	80°
1020 nm						
Longyeab	0.70	1.20	1.90	0.70	0.80	0.90
Greenland	0.70	0.90	–	0.70	0.72	–
Antarctica	0.65	0.90	–	0.65	0.67 (30°)	–
670/440 nm						
Longyeab	0.90	1.20	1.65	0.90	0.98	1.00
Greenland	0.93	1.05	–	0.92	0.92	–
Antarctica	0.91	1.06	–	0.90	0.91 (30°)	–

Title Page

Abstract | Introduction

Conclusions | References

Tables | Figures

◄◄ | ►►

◄ | ►

Back | Close

Full Screen / Esc

Printer-friendly Version

Interactive Discussion

Table 2. Main characteristics of the ice drift datasets available from the Damocles project. Grid spacing: spacing between ice motion vectors, time span: duration of the observed motion, area averaging: extent of the area of sea ice that is monitored by each motion vector.

Product	Source Institution	Instrument/ Mode	Grid Spacing	Time Span	Area Averaging
OSI-405	OSI SAF	SSM/I, AMSR-E, ASCAT	62.5 km	48 h	$\sim 140 \times 140\,km^2$
IFR-Merged	IFREMER/ Cersat	SSM/I, QuikSCAT, ASCAT	62.5 km	72 h	$\sim 140 \times 140\,km^2$
IFR-89GHz	IFREMER/ Cersat	AMSR-E 89 GHz H/V	31.25 km	48 h	$\sim 70 \times 70\,km^2$
OSI-407	OSI SAF	AVHRR band 2/4	20 km	24 h	$\sim 40 \times 40\,km^2$
DTU-WSM	DTU	ASAR-WSM	10 km	24 h	$\sim 10 \times 10\,km^2$
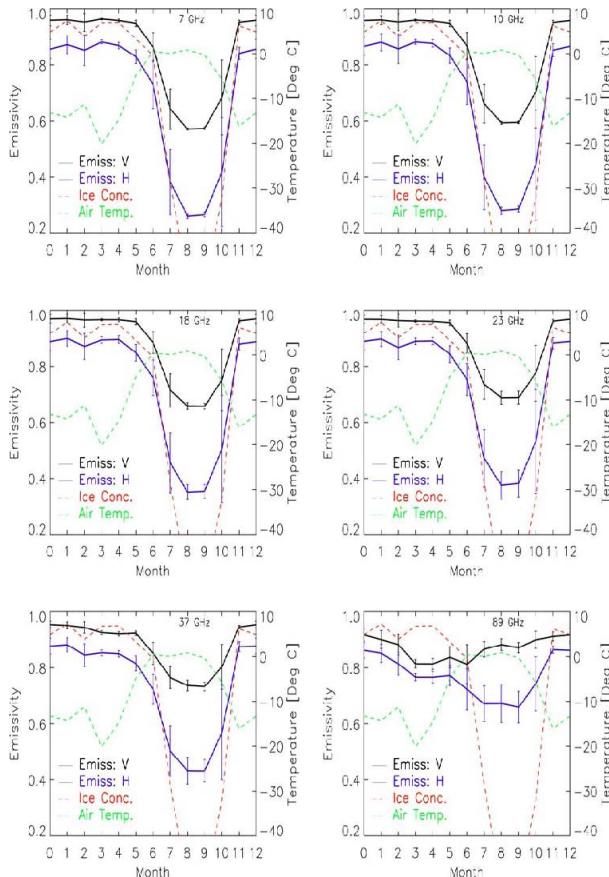
Fig. 1. Seasonal variation of emissivities of first-year ice at AMSR-E frequencies, (black) vertical and (blue) horizontal polarizations. (Top left) 7 GHz, 10 GHz, 18 GHz, 23 GHz, 37 GHz, and (bottom right) 89 GHz. Red dashed line: ice concentration. Green dashed line: air temperature. Months 0 and 12 are the same.

Title Page

Abstract | Introduction

Conclusions | References

Tables | Figures

|◄ | ►|

◄ | ►

Back | Close

Full Screen / Esc

Printer-friendly Version

Interactive Discussion
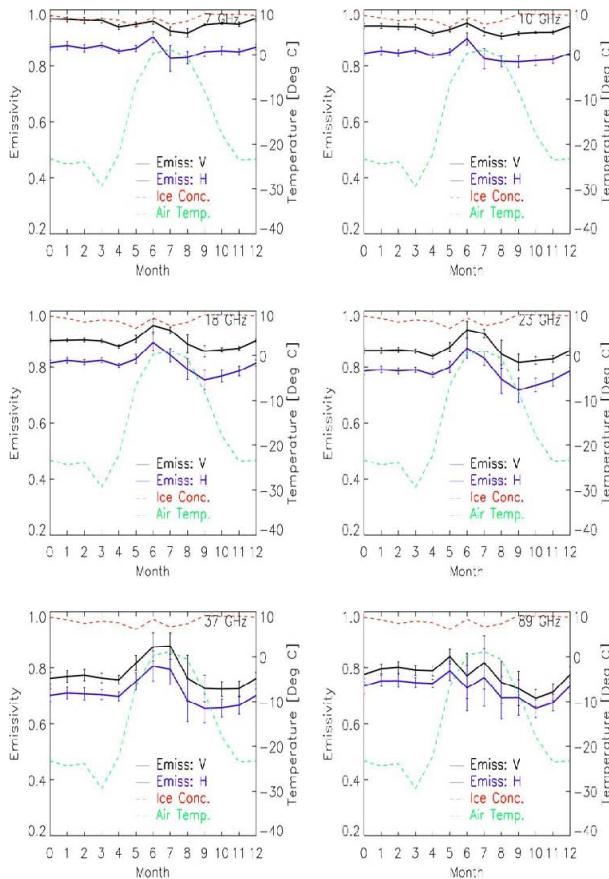
Fig. 2. Seasonal variation of emissivities of multiyear ice at AMSR-E frequencies ((black) vertical and (blue) horizontal polarizations). (Top left) 7 GHz, 10 GHz, 18 GHz, 23 GHz, 37 GHz, and (bottom right) 89 GHz. Red dashed line: ice concentration. Green dashed line: air temperature. Months 0 and 12. From Mathew et al. (2009).

Remote sensing of sea ice during DAMOCLES

G. Heygster et al.

Title Page	
Abstract	Introduction
Conclusions	References
Tables	Figures
◄◄	►►
◄	►
Back	Close
Full Screen / Esc	
Printer-friendly Version	
Interactive Discussion	
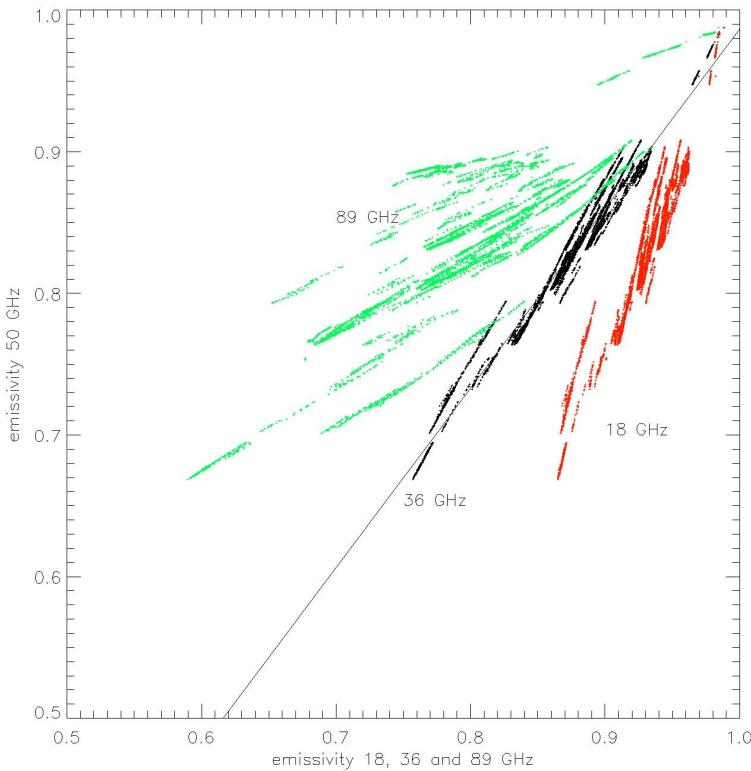
Fig. 3. The simulated 18, 36 and 89 GHz emissivity at vertical polarisation of multiyear ice vs. the 50 GHz emissivity. The 18 GHz vs. the 50 GHz emissivity is shown in red, the 36 GHz vs. the 50 GHz in black, and the 89 GHz vs. the 50 GHz in green. The line is fitted to the 36 GHz vs. 50 GHz cluster: $e_{v\,50} = 1.268\,e_{v\,36} - 0.28$.
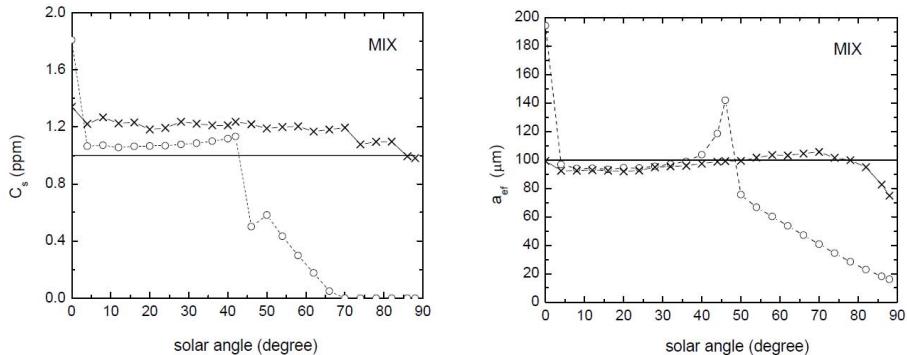
Fig. 4. Retrieval of effective snow grain size and soot concentration by two methods: SGSP (−x) and LUT-Mie (o). Nadir observation. Horizontal lines mark true values.

Full Screen / Esc

RossIceshelf 2010 Jan 22
Aqua MODIS snow grain size, 2010 Jan 22 07:20 UTC
AMSR–E ASI ice concentration isolines: 30%, 60%, 90%
© University of Bremen (2010 Jul 28 13:22 UTC)

Grainsize[micrometer]
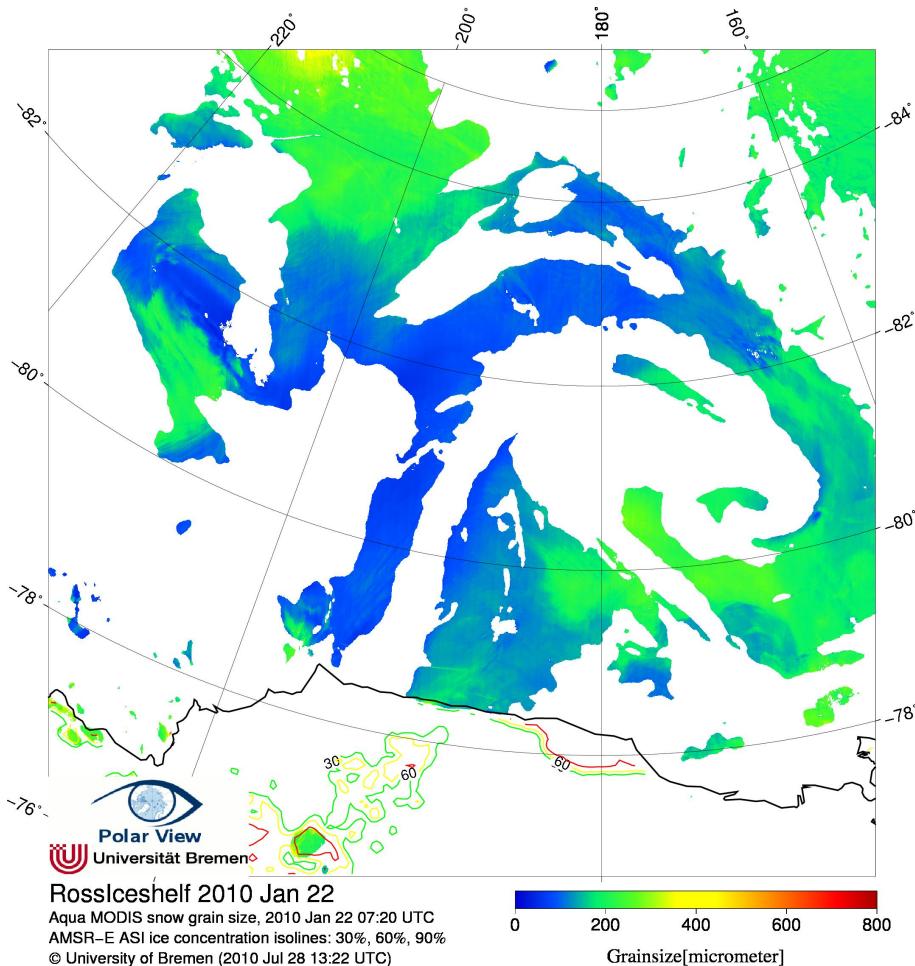
Fig. 5. Snow grain size retrieval example on the Ross ice shelf as provided in near real time.
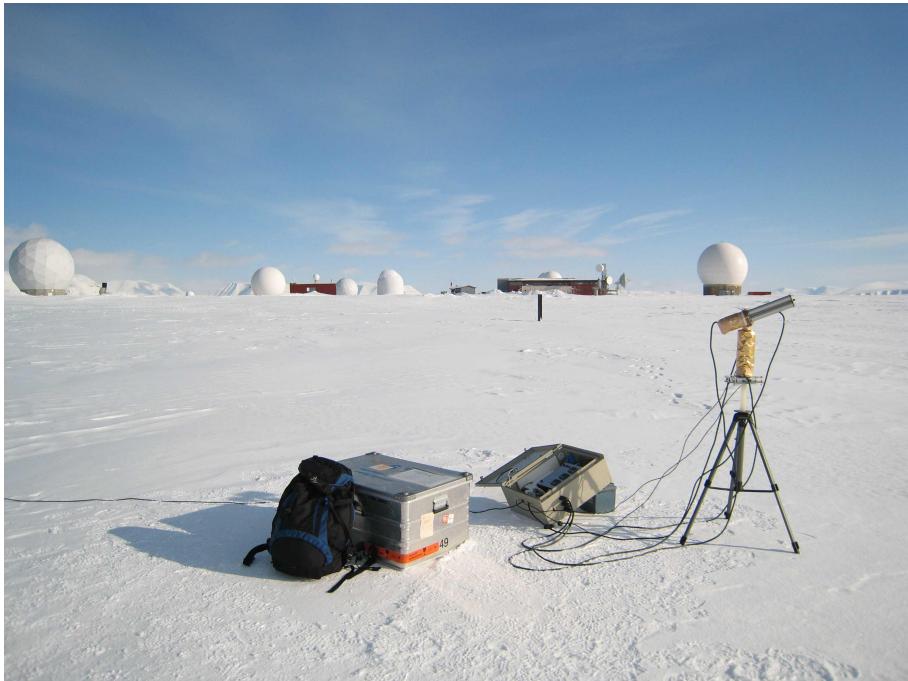
Fig. 6. Observation site at Longyearbyen, Svalbard.
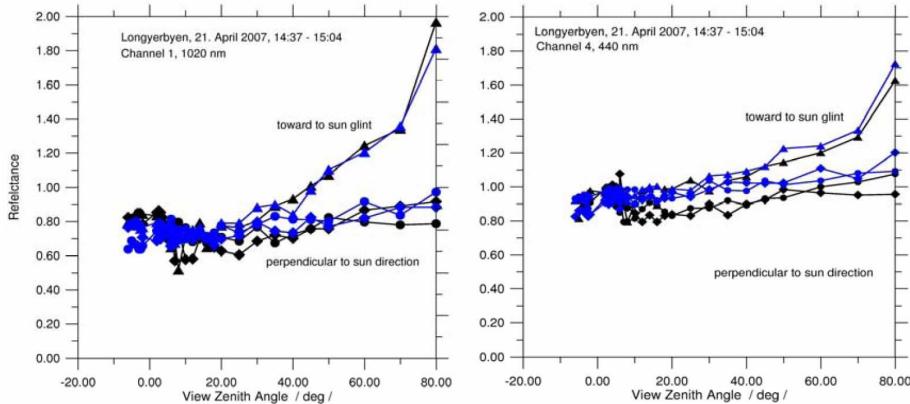
Fig. 7. Snow reflectance functions taken in Longyearbyen at 1020 nm (left) and 440 nm (right). Different curves represent different measurements.
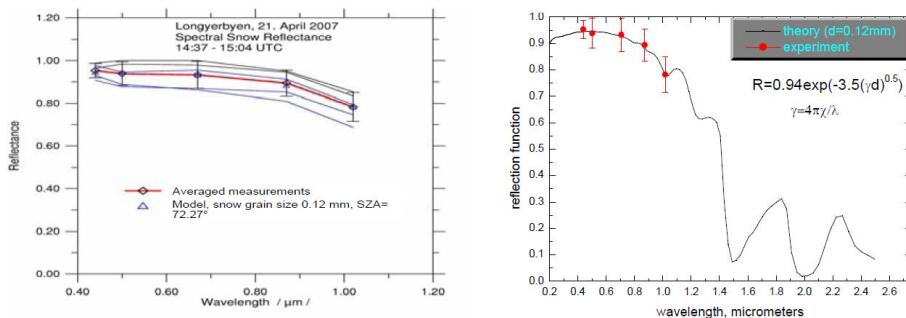
Fig. 8. **(a)** all observed reflectances, together with those obtained from the snow forward model of Kohanovsky (2011) with effective grain size 0.12 mm, **(b)** observed and modelled (Kohknaovsky et al., 2011) snow reflectance.
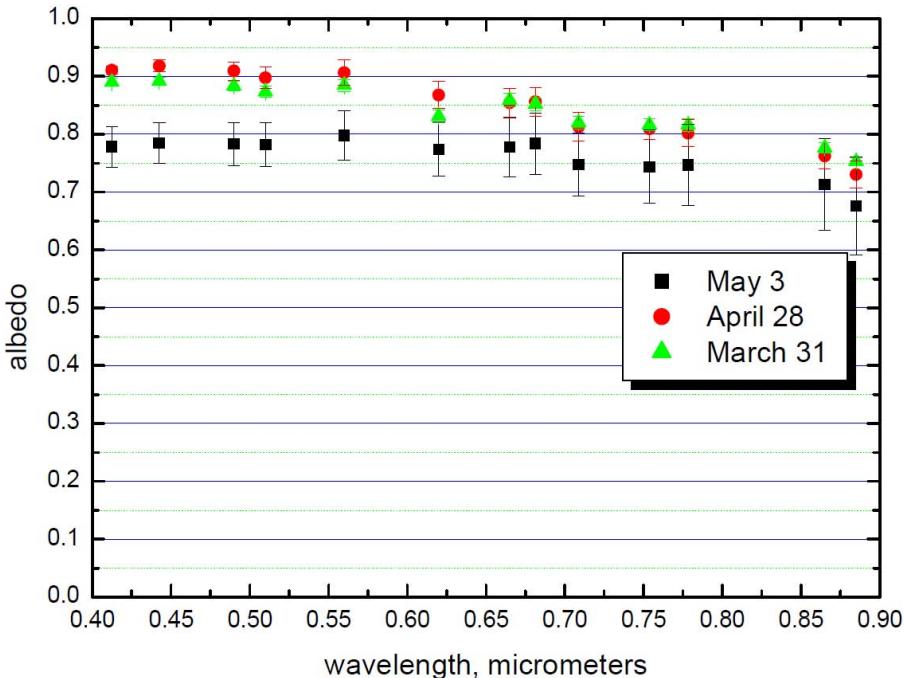
Fig. 9. The albedo retrieved from MERIS observations for several days in 2006 (average for all orbits). As it should be, albedo decreases with the wavelength and it is smaller for days with higher temperature. The results for the point with the coordinates (24.6° E, 79.8° N) is given (glacier Austfonna, island Nordaustlandet on Spitsbergen).

◄◄	►►
◄	►
Back	Close

Full Screen / Esc

Printer-friendly Version

Interactive Discussion
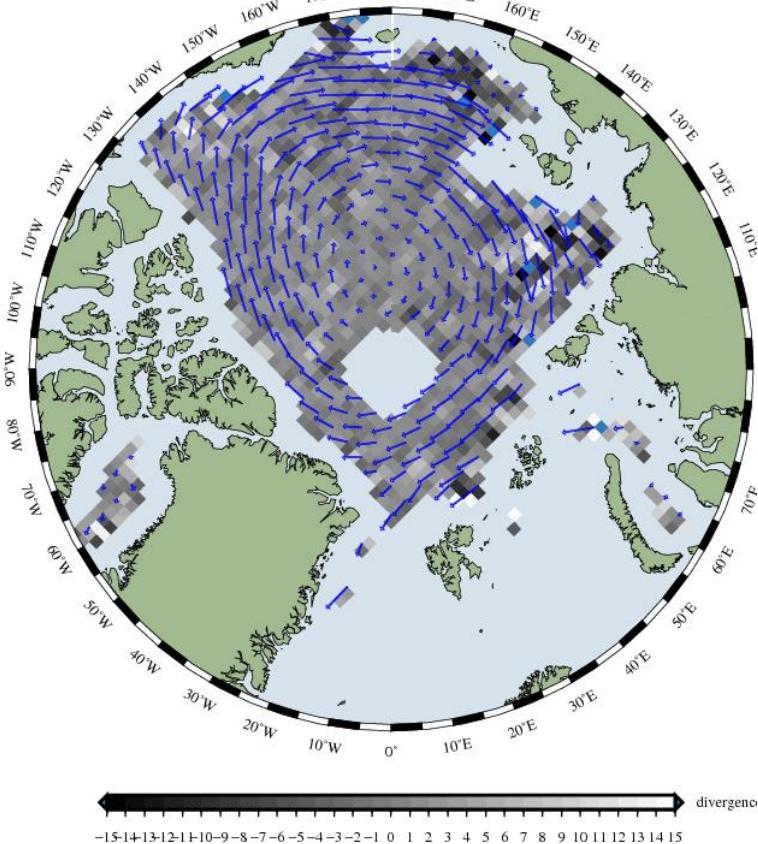
Fig. 10. Arctic sea ice deformation (in percent) between the days 20100221 and 20100223, calculated from AMSR ice drift data. Shades of greys indicate divergence (white) and convergence (dark) areas.

**Remote sensing of
sea ice during
DAMOCLES**

G. Heygster et al.
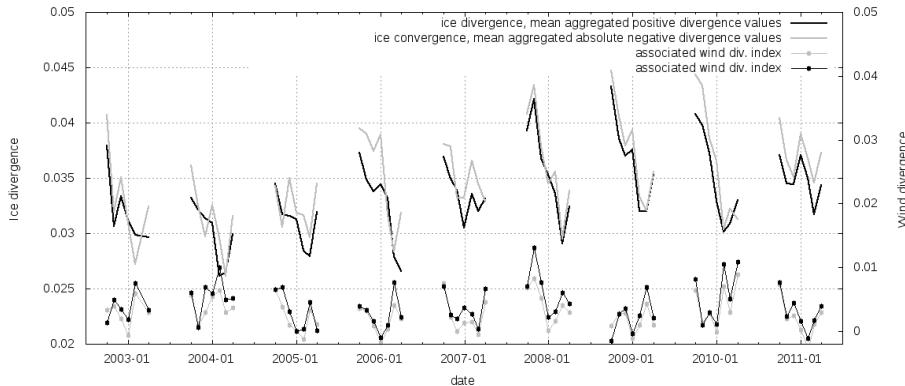
Fig. 11. Monthly mean values of Arctic sea ice divergence and convergence, during seven winter month since 2002 (black and gray lines, respectively). A corresponding surface wind divergence index is plotted using lines with points. The ice convergence values are negative divergence values, but plotted here as absolute values for easy comparison to positive divergence values.

Title Page

Abstract | Introduction

Conclusions | References

Tables | Figures

◀◀ | ▶▶

◀ | ▶

Back | Close

Full Screen / Esc

Printer-friendly Version

Interactive Discussion
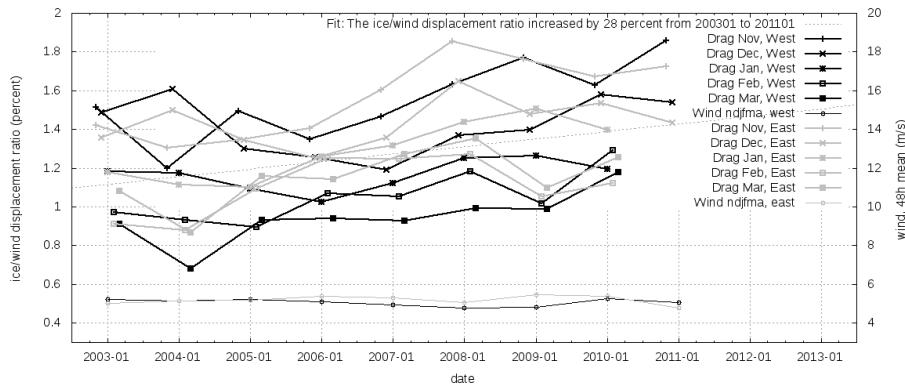
Fig. 12. Monthly mean ice/wind displacement ratios, November to March (200211–201012), divided into the Western and Eastern Arctic regions (black and grey, respectively). The two thin lines at the bottom of the figure show the corresponding 48 h wind speed as winter mean values.

Remote sensing of sea ice during DAMOCLES

G. Heygster et al.

Title Page

Abstract | Introduction

Conclusions | References

Tables | Figures

◄◄ | ►►

◄ | ►

Back | Close

Full Screen / Esc

Printer-friendly Version

Interactive Discussion
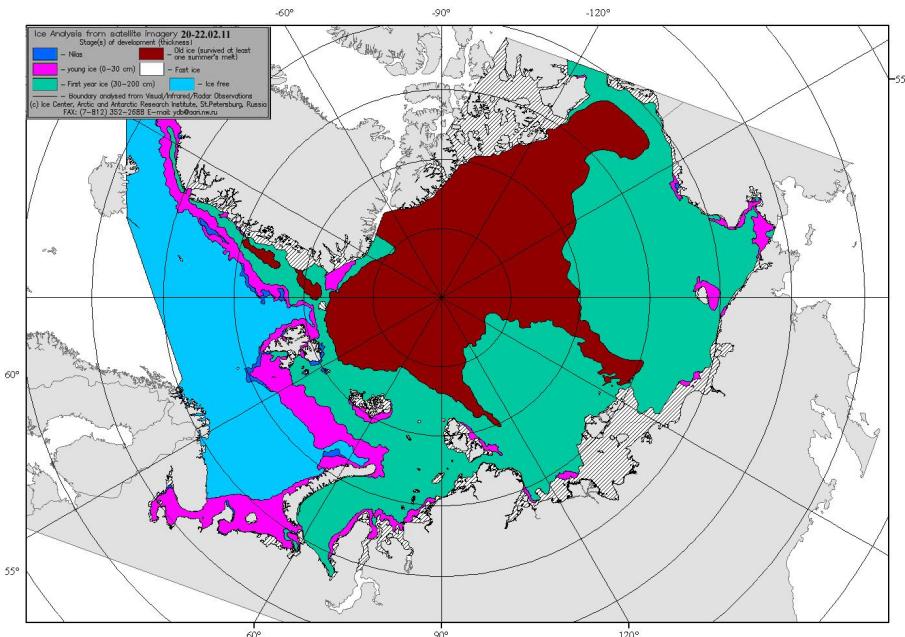
Fig. 13. The Arctic Ocean ice chart for the period 20–22 February 2011, issued by Arctic and Antarctic Research Institute.